PAPER

Check for updates

Improvement in luminescent properties and thermo-optical conversion mechanism of Na₂SiF₆:Mn⁴⁺,K⁺@GQDs

Xue Zhong,[a] Tianman Wang,[a] Yuelan Li,[a] Yan Yu,[a] Long Chen,[a] Sen Liao, [iD] *[ab] Yingheng Huang*[ab] and Jinqiao Long*[c]

Herein, a series of NSF:0.05Mn⁴⁺,0.04K⁺@GQD (NSF: Na₂SiF₆, GQDs: Cl-containing graphene quantum dot) phosphors was prepared. Double enhancement effects on the luminescent intensity and thermal stability triggered by the GQD coating were observed for the optimal sample as follows: (a) its PL intensity was 1.72 times that of the uncoated control sample and (b) its luminescent thermal stability was greatly enhanced, with integrated PL intensities of 120, 150 and 180 °C to 179.7%, 175.8%, and 119.3% of the initial value at 25 °C, respectively. It is proposed that the above-mentioned behaviors involve a change in some of the thermal energy into light energy *via* a phonon-induced mechanism. The thermal stability analysis results showed that the optimal sample is suitable for application in high-power WLEDs. Specifically, warm white light with a low correlated color temperature, high luminescent efficiency and high color rendering index was obtained from the prototype WLEDs using the optimal sample as a red-emitting component.

1 Introduction

Presently, commercial white light-emitting diodes (WLEDs) are assembled with a blue-emitting LED chip and Y₃Al₅O₁₂:Ce³⁺ (YAG:Ce) yellow-emitting phosphor. However, due to the lack of a red-emitting component, they have obvious disadvantages. These disadvantages are: the color rendering index (CRI < 80) is low and the correlated color temperature (CCT) is high, which obviously affect the quality of white light and limit its application.[1–3] Thus, to further improve the luminescent characteristics of WLEDs, the selection and preparation of red phosphors and optimization of their performance have become a research hotspot in the field of WLEDs, attracting increasing attention.[1] Mn⁴⁺-Doped fluoride red-emitting phosphors with formulas A₂XF₆:Mn⁴⁺ or BXF₆:Mn⁴⁺ (A = K, Na, Rb and Ce; B = Ba and Zn; *x* = Si, Ge, Zr, Ti) have attracted widespread attention due to their excellent strong broad-band excitation in the blue light region, strong narrow-band emission in the red light region, low phonon energies, high chemical stability, and diverse structures.[4–10] However, they still have several shortcomings that

[a]School of Chemistry and Chemical Engineering, Guangxi University, Nanning, Guangxi, 530004, China. E-mail: liaosen@gxu.edu.cn; Fax: +86 771 3233718; Tel: +86 771 3233718

[b]Guangxi Key Laboratory of Processing for Non-ferrous Metals and Featured Materials, School of Resources, Environment and Materials, Guangxi University, Nanning, Guangxi, 530004, China

[c]Guangxi Colleges and Universities Key Subject of Material Physics and Chemistry, College of Chemistry & Environment Engineering, Baise University, Baise, Guangxi, 533000, China

need to be overcome:[11] Firstly, the luminescent intensity of Mn⁴⁺-doped fluoride phosphors is not sufficiently strong, causing the mass ratio of the phosphor to YAG:Ce phosphor to be as high as 2–3 in practical application.[11] Secondly, the working temperature range of WLEDs is 150 to 180 °C, but the luminescent intensity of phosphors will be obviously reduced due to thermal quenching, and thus their thermal stability also needs to be improved.[12] Thirdly, the [MnF₆]²⁻ activator in these phosphors easily hydrolyze under humid conditions, leading to the loss of their emission;[13–15] therefore, their water resistance also needs to be further improved.

It is interesting that some of Mn⁴⁺-doped phosphors have good luminescent thermal stability at about 150 °C, which is induced by their negative thermal quenching behavior.[12,16–18] For example, the integrated emission intensity of K₂SiF₆:Mn⁴⁺ coated with a thin Al₂O₃ layer is about 104.6% of the initial value.[16] The integrated emission intensity of the K₂(Ge₁₋ₓSiₓ)F₆:Mn⁴⁺ (*x* = 0.3) phosphor showed an enhancement at 152 °C, which increased by 117% of the initial value.[17] The red-emitting phosphor Rb₂TiF₆:Mn⁴⁺ was synthesized *via* the ion exchange method under mild conditions and exhibited a noteworthy luminescent enhancement with an increase in temperature, where its integrated emission intensity at 150 °C was enhanced to about 120% of the initial value.[18] CsMoO₂F₃:Mn⁴⁺ synthesized *via* the simple co-precipitation method showed high luminescent stability.[12] The results of luminescent measurement at different temperatures showed that its integrated emission intensity at 150 °C was 129% that of the initial value.[12] However, actually, most Mn⁴⁺-doped fluoride phosphors exhibit

thermal quenching before 125 °C, and thus show poor thermal stability.[19–23] Consequently, this defect shortens the service life of WLEDs and severely restricts their industrial applications. Therefore, the development of new Mn^{4+}-doped fluoride phosphors with higher inherent luminescent thermal stability is still highly desirable.

In addition, most Mn^{4+}-doped fluoride phosphors are prepared using $KMnO_4$ and H_2O_2 as the starting materials,[24,25] where the activator K_2MnF_6 is formed by the reaction of $KMnO_4$ and H_2O_2. However, the reaction is too violent to be applied in industry. Thus, to avoid the violent reaction, some Mn^{4+}-doped fluoride phosphors have been prepared without the use of H_2O_2 as a reducing agent.[14,26,27] For example, $K_2XF_6:Mn^{4+}$ (X = Ti, Si and Ge) phosphors were successfully prepared via a H_2O_2-free chemical co-precipitation method using XO_2 (X = Ti, Si and Ge), acetic acid glacial, HF, $KMnO_4$ and KF as the starting materials.[26] $Na_2XF_6:Mn^{4+}$ (X = Si, Ge, and Ti) phosphors were synthesized via a simple H_2O_2-free co-precipitation method using SiO_2, TiO_2, GeO_2, NaF, HF, and $NaMnO_4\cdot H_2O$ as raw materials.[16] $K_2TiF_6:Mn^{4+}$ phosphors were obtained via the H_2O_2-free etching of $Ti(OC_4H_9)_4$ in HF solution with $KMnO_4$ and KF as starting materials.[27] $K_{2x}Ba_{1-x}TiF_6:Mn^{4+}$ phosphors with high luminescent efficiency, high luminescent thermal stability and good water proof ability were synthesized via a facile H_2O_2-free hydrothermal method using KCl, $BaCl_2\cdot 2H_2O$, $KMnO_4$, H_2TiF_6 and HF as raw materials.[14]

In conclusion, many achievements have been made in preparing Mn^{4+}-doped fluoride phosphors through H_2O_2-free methods.[14,16,26,27] In these methods, the activator K_2MnF_6 (or Na_2MnF_6) is obtained via the self-redox of $KMnO_4$ ($NaMnO_4$) in KF–HF solution, and H_2XF_6 (X = Ti, Si and Ge) is produced with XO_2 (X = Ti, Si and Ge), $Ti(OC_4H_9)_4$ and H_2TiF_6 as raw materials. The final products are $BaXF_6$ or A_2XF_6 (A = K, Na; X = Ti, Si and Ge). Thus, based on the above-mentioned reports, it is feasible to use Na_2SiF_6 as a raw material in the H_2O_2-free method. Therefore, herein, $Na_2SiF_6:K^+,Mn^{4+}$ phosphors were synthesized via an H_2O_2-free method using $Na_2SiF_6:K^+$ as the raw material.

Due to their high surface area, conjugated large π bonds, wide applications, environment friendliness, and high thermal stability, carbon-based monolayer nanosheets, such as graphene, graphite oxide (GO), reduced graphene oxide (rGO) and GQDs are considered advanced functional carbon nanomaterials.[28–30] Thus, many research efforts have been focused on using carbon nanomaterials. It is interesting that the luminescence of some rare earth compounds can be significantly enhanced by carbon nanosheets. For example, the luminescence of Eu^{3+}–TC complexes (TCs: tetracyclines) was significantly enhanced by GQDs, where the emission intensity of Eu^{3+}–TCs–GQDs was 12.1 times that of Eu^{3+}–TCs.[28] When beta-$NaYF_4:Gd^{3+}/Tb^{3+}$ was coated with GQDs, the emission intensity of the coated sample was 7.5 times that of the uncoated control sample.[29] Furthermore, it is encouraging is that after the $SrBaSi_2O_2N_2:Eu^{2+}$ phosphor was coated by rGO, the long-range thermal stability of the coated sample was enhanced compared with that of the uncoated control sample.[30]

In conclusion, given that the coating of GQDs or rGO can enhance the luminescent intensity or thermal stability of rare

earth compounds or rare earth-doped phosphors, then similarly, the coating of GQDs or rGO may also enhance the luminescent intensity or luminescent thermal stability of Mn^{4+}-doped fluoride phosphors.

In our previous work, $K_2SiF_6:Mn^{4+}@GQDs$ was synthesized via an H_2O_2-free hydrothermal method.[31] As a part of our ongoing research, herein, based on the H_2O_2-free ion exchange method, an efficient strategy was explored for the synthesis of $Na_2SiF_6:Mn^{4+},K^+@GQDs$ phosphors. The experimental results showed that the luminescent intensity and thermal stability of the coated sample were enhanced simultaneously. Also, the mechanism responsible for this enhancement was explored.

2 Experimental and methodology

2.1 Reagent and apparatus

Cl-Containing graphene quantum dots (CGQDs) were purchased from Nanjing XFNANO Materials Tech Co. Ltd, China, and used without further purification. In addition, most chemicals were reagent-grade pure and purchased from Sinopharm Chemical Reagent Co. Ltd, China. The elemental contents of the sample were determined using a PerkinElmer Optima 3100 RL inductively coupled plasma atomic emission spectrometer (ICP-AES). Firstly, the samples were dissolved in 10 mL of 1 : 1 HCl aqueous solution containing several drops of H_2O_2 (30%). Secondly, the solution was diluted to 100 mL with deionized water. Thirdly, the metal elemental contents in the solution were examined with ICP-AES. X-ray diffraction (XRD) was performed at a scanning rate of 5° min^{-1} in the 2θ range of 5° to 70° at room temperature using a Rigaku D/max 2500 V diffractometer equipped with a graphite monochromator by utilizing monochromatic CuKα radiation (λ = 0.154178 nm). The morphologies of the samples were examined using a Hitachi S-3400 scanning electron microscope (SEM) with an attached energy-dispersive X-ray spectrometer (EDS) at the accelerating voltage of 10.0 kV. The samples were mounted on an aluminum slice coated with Au. The photoluminescence excitation (PLE) and emission (PL) spectra were recorded at room temperature using a Horiba Fluoro Max-4-R F6000 spectrophotometer equipped with a xenon lamp as the excitation source. The luminescence decay curve and the photoluminescence quantum yield were obtained using an Edinburgh FLS980 fluorescence spectrophotometer. Fourier transform infrared spectroscopy (FT-IR) was performed using a Bruker Tensor 27 Spectrometer (Germany) with a KBr disc in the wavelength range of 4000–400 cm^{-1}. Thermogravimetry (TG) measurements were performed using a NETZSCH STA 409 PC/PG thermogravimetric analyzer. Pure nitrogen gas (99.999%) was used as protective atmosphere with a flow rate of 20 mL min^{-1}. Sample powders with a mass of 8 ± 0.1 mg were used for the experiments with heating rates of 10 °C min^{-1}. The samples were loaded without pressing into a corundum crucible. The performance of the WLEDs was measured using an auto-temperature LED opto-electronic analyser (LATA-1000, Everfine). X-ray photoelectron spectroscopy (XPS) was performed using a Thermo Scientific K-Alpha X-ray photoelectron spectrometer.

2.2 Preparation of samples

2.2.1 Na$_2$SiF$_6$:xK$^+$.
Na$_2$SiF$_6$:0.04K$^+$ was synthesized as follows: (1) 7.20 g (68.6 mmol) Na$_2$CO$_3$ and 0.20 g (1.4 mmol) K$_2$CO$_3$ were mixed to obtain a mixed powder. (2) The mixed powder was added to 20.17 g (140 mmol) H$_2$SiF$_6$ (50%) solution slowly with stirring. The mixture was ground in an agate mortar for 60 min. (3) The mixture was kept at 90 °C for 3 h and dried at 120 °C for 3 h to yield Na$_2$SiF$_6$:0.04K$^+$ (NSF:0.04K$^+$). Synthetic procedures for Na$_2$SiF$_6$:xK$^+$ samples with (x = 0.02–0.12) are the same as that of NSF:0.04K$^+$.

2.2.2 Na$_2$SiF$_6$:yMn^{4+}.
Firstly, 0.24 g (1.5 mmol) powder of KMnO$_4$, 15 mL HF (40%) and 0.5 g KF·2H$_2$O were put in a 50 mL plastic beaker and stirred for 30 min with a magnetic stirrer to get a mixture (I). Secondly, 4.47 g (23.75 mmol) powder of Na$_2$SiF$_6$ (y = molar ratio of Mn/(Mn + Si) = 0.05) was added to mixture (I) and stirred for 48 h. Thirdly, the precipitate was collected, filtered and washed with acetone several times and dried at 70 °C for 3 h to get sample (i) Na$_2$SiF$_6$:y_1Mn^{4+} (NSF:yMn^{4+}, y_1 = 0.05). The synthetic procedures for the NSF:yMn^{4+} samples with (y = 0.01–0.11) are as the same as that for NSF:y_1Mn^{4+}.

2.2.3 NSF:y_1Mn^{4+},xK$^+$.
Firstly, 0.24 g (1.5 mmol) powder of KMnO$_4$, 15 mL HF (40%) and 0.5 g KF·2H$_2$O were put in a 50 mL plastic beaker and stirred for 30 min with a magnetic stirrer to get a mixture. Secondly, 5.38 g (28.5 mmol) powder of NSF:0.04K$^+$ was added to the mixture and stirred for 48 h. Thirdly, the precipitate was collected, filtered and washed with acetone several times and dried at 70 °C for 3 h to get sample (ii) (NSF:y_1Mn^{4+},0.04K$^+$). The synthetic procedures for NSF:y_1-Mn^{4+},xK$^+$ with (x = 0.02–0.14) are as the same as that of NSF:y_1Mn^{4+},0.04K$^+$.

2.2.4 Na$_2$SiF$_6$:y_1Mn^{4+},0.04K$^+$@GQDs$_{z\text{ mg mol}^{-1}}$.
The steps for the synthesis of the Na$_2$SiF$_6$:y_1Mn^{4+},0.04K$^+$@GQDs$_{8\text{ mg mol}^{-1}}$ (NSF:0.05Mn^{4+},0.04K$^+$@GQDs$_{8\text{ mg mol}^{-1}}$) sample are as follows: Firstly, 10 mL HF (40%) solution and 3.89 g (20 mmol) NSF:y_1Mn^{4+},0.04K$^+$ were added to a 50 mL hydrothermal reactor and completely mixed with stirring. Secondly, after stirring for 30 min, a GQD solution (solution obtained by mixing 160 μL GQDs (1 mg mL^{-1}) and 5 mL HF (40%) solution) was dropped into the mixture with stirring. Thirdly, the hydrothermal tank was kept in an oven for 3 h at 120 °C. Then, the autoclave was taken out of the oven and cooled naturally to room temperature. Finally, the yellow precipitate was collected, washed with acetone several times and dried at 70 °C for 3 h to get sample (iii), NSF:y_1Mn^{4+},0.04K$^+$@GQDs$_{8\text{ mg mol}^{-1}}$. The synthetic procedures for NSF:y_1Mn^{4+},0.04K$^+$@GQDs$_{z\text{ mg mol}^{-1}}$ with (z = 1–14 mg mol^{-1}) are as the same as that of NSF:y_1Mn^{4+},0.04K$^+$@GQDs$_{8\text{ mg mol}^{-1}}$.

3 Results and discussion

3.1 Structure, morphology and composition analyses

The results of the ICP analysis for samples (i)–(iii) are shown in Table 1, where the corresponding molecular formulae of samples (i)–(iii) are NSF:0.05Mn^{4+}, NSF:0.05Mn^{4+},0.04K$^+$ and NSF:0.04Mn^{4+},0.04K$^+$@GQDs$_{8\text{ mg mol}^{-1}}$, respectively. The results

show that NSF:0.04Mn^{4+},0.04K$^+$ was coated by GQDs in sample (iii).

The results show that: (a) under the above-mentioned reaction conditions, after reaction for 48 h, KMnO$_4$ was basically transformed into K$_2$MnF$_6$, and then K$_2$MnF$_6$ was doped into samples (i)–(iii) immediately and (b) samples (ii) and (iii) were further doped with K$^+$.

The chemical process for the synthesis of sample (i) (NSF:0.05Mn^{4+}) from the reactants is represented by the following formulae.

$$4\text{KMnO}_4 + 4\text{KF} + 20\text{HF} = 4\text{K}_2\text{MnF}_6 + 10\text{H}_2\text{O} + 3\text{O}_2 \quad (1)$$

$$y\text{K}_2\text{MnF}_6 + (1 - y)\text{Na}_2\text{SiF}_6 = (1 - y)\text{Na}_2\text{SiF}_6{:}y\text{K}_2\text{MnF}_6 \quad (2)$$
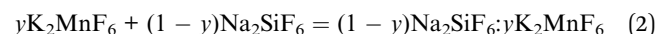
Formula (1) shows that KMnO$_4$ undergoes its own redox reaction in acidic conditions and forms K$_2$MnF$_6$. Formula (2) is the reaction for the formation of NSF:yMn^{4+}.

Fig. 1 shows the XRD patterns of the three as-synthesized samples: (i) NSF:0.05Mn^{4+}, (ii) NSF:0.05Mn^{4+},0.04K$^+$, (iii) NSF:0.05Mn^{4+},0.04K$^+$@GQDs$_{8\text{ mg mol}^{-1}}$. In Fig. 1a, all the diffraction peaks of the three samples were indexed using the Jade 6.5 software and in agreement with the hexagonal Na$_2$SiF$_6$ phase standard data (PDF #72-1115) with the space group P321 (150) (Table 2). The crystal structure of sample (i) is shown in Fig. 1b, where Na$^+$ and Ti^{4+} are each coordinated to six F$^-$ ions, respectively, forming octahedra. These alternating oblique arrangements of the [NaF$_6$] and [SiF$_6$] (Fig. 1c) octahedra result in low symmetry and the formation of efficient red emissions. Furthermore, Mn^{4+} and Si^{4+} have the same valence (4+) and similar ionic radii (r = 0.40 Å for Si^{4+} and r = 0.53 Å for Mn^{4+}), and thus Mn^{4+} is incorporated in the Si^{4+} site and evenly distributed in the lattice, forming [MnF$_6$]$^{2-}$ octahedra, which allow Mn^{4+} to have sufficient coordination field stabilization energy. The lattice parameters of the samples obtained from the indexed results are listed in Table 2. Fig. 1a shows that the samples have high crystallinity without other impurities. Given that the mass percentage of GQDs in the sample (iii) is too small (about 0.0042%) to be detected, the peaks of GQDs were not observed. Table 1 shows that the volume size of the samples follows the order of (iii) > (ii) > (i) > PDF #72-1115. The results indicate that: (a) some Si^{4+} ions (CN = 6, r = 0.40 Å)[13] in the lattice sites are replaced by Mn^{4+} ions (CN = 6, r = 0.53 Å).[13] (b) Some Na$^+$ ions (r = 1.18 Å)[32] in the lattice sites are replaced by K$^+$ ions (r = 1.38 Å)[33] in the sample (ii). (c) GQDs coordinated with

Table 1 Refined lattice parameters and volumes of the three samples[a]

	$a = b$/Å	c/Å	γ/°	$a = \beta$/°	V/Å^3
PDF #72-1115	8.859	5.038	120	90	342.43
(i)	8.86072	5.04085	120	90	342.75
(ii)	8.86530	5.04365	120	90	343.29
(iii)	8.86681	5.04392	120	90	343.43

[a] (i) NSF:0.05Mn^{4+}, (ii) NSF:0.05Mn^{4+},0.04K$^+$, and (iii) NSF:0.05Mn^{4+},0.04K$^+$@GQDs$_{8\text{ mg mol}^{-1}}$.
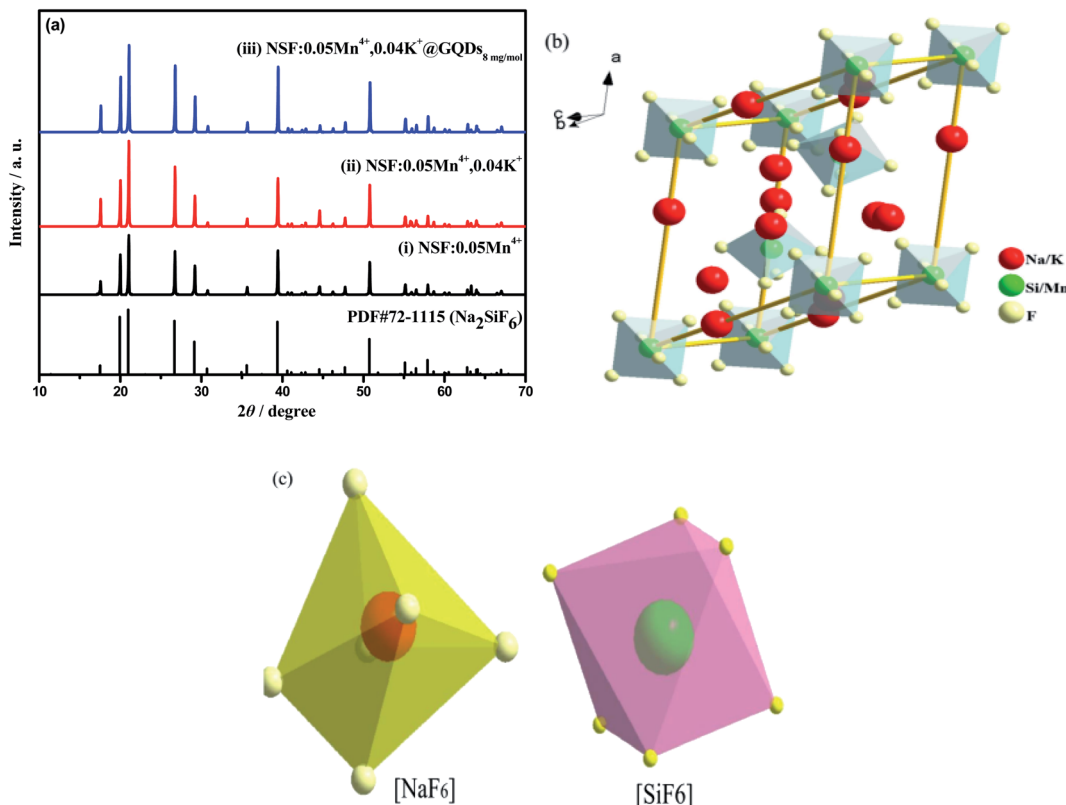
Fig. 1 XRD patterns of the three samples, (i) NSF:0.05Mn^{4+}, (ii) NSF:0.05Mn^{4+},0.04K$^+$, (iii) NSF:0.05Mn^{4+},0.04K$^+$@GQDs$_{8\ mg\ mol^{-1}}$: (a) full XRD patterns. (c) and (d) Crystal structure of sample (ii).

Table 2 Comparison of the negative thermal quenching of some samples[a]

Sample	Initial integrated intensity/%	120 °C/%	150 °C/%	180 °C/%	Ref.
K$_3$AlF$_6$:Mn^{4+}	100	210	200	140	11
CsMoOF:Mn^{4+}	100	120	129	114	15
K$_2$SiF$_6$:Mn^{4+}	100	109	112	110	43
KSF:Mn@GQDs	100	157	150	126	48
K$_2$SiF$_6$:Mn^{4+}	100	149	167	186	49
Sample (i)	100	75	49	23	This work
Sample (ii)	100	114	101	59	This work
Sample (iii)	100	180	176	119	This work

[a] (i) NSF:0.05Mn^{4+}, (ii) NSF:0.05Mn^{4+},0.04K$^+$, and (iii) NSF:0.05Mn^{4+},0.04K$^+$@GQDs$_{8\ mg\ mol^{-1}}$.

Mn^{4+} or Si^{4+}, resulting in a further slight increase in volume for sample (iii).

The SEM images, EDS, XPS and FTIR spectra of samples (ii) and (iii) ((ii) NSF:0.05Mn^{4+}, 0.04K$^+$ and (iii) NSF:0.05Mn^{4+},0.04K$^+$@GQDs$_{8\ mg\ mol^{-1}}$) are shown in Fig. 2. Fig. 2a shows that crystal morphologies of sample (ii) are irregular particles with a size of about 10 μm, which are clustered together with small irregularly shaped particles (Fig. 2a). Fig. 2b clearly shows that the surface of sample (iii) is adhered with tiny sheets, implying that the GQDs were successfully deposited on the surface of sample (iii).

The EDS spectra of the samples are shown in Fig. 2c and d. Fig. 2c shows that: (a) sample (ii) is composed of elements of Na, K, Si, Mn, F and C, and the peak of C is a weak one, which is attributed to CO$_2$ adsorbed from the air. (b) Sample (iii) is composed of elements of Na, K, Si, Mn, F and C (Fig. 2d), and the peak of C is stronger than that of sample (ii), which is due to the overlap of the peak for the GQDs and CO$_2$ adsorbed from the air. Thus, the result in Fig. 2d indicates that the GQDs were successfully coated on the surface of sample (iii).

To further determine the element composition of the samples, their XPS energy and FTIR spectra were measured. The XPS energy spectra of samples (ii) and (iii) are shown in Fig. 2e.
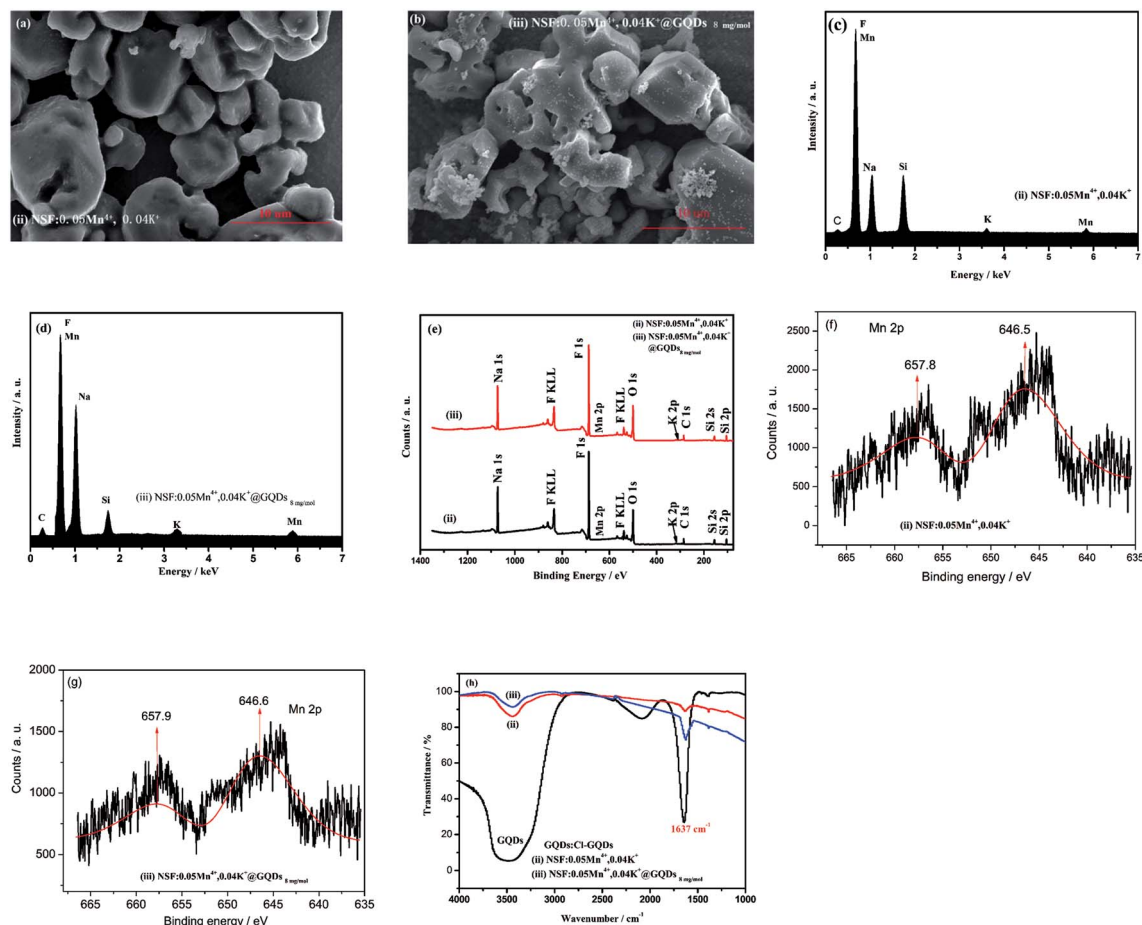
Fig. 2 SEM images, EDS, XPS and FTIR spectra of two samples, (ii) NSF:0.05Mn^{4+},0.04K$^+$ and (iii) NSF:0.05Mn^{4+},0.04K$^+$@GQDs$_{8 mg mol^{-1}}$: (a) and (b) SEM images of samples (ii) and (iii). (c) and (d) EDS spectra. (e) XPS spectra. (f) and (g) High-resolution XPS of Mn 2p. (h) FTIR spectra.
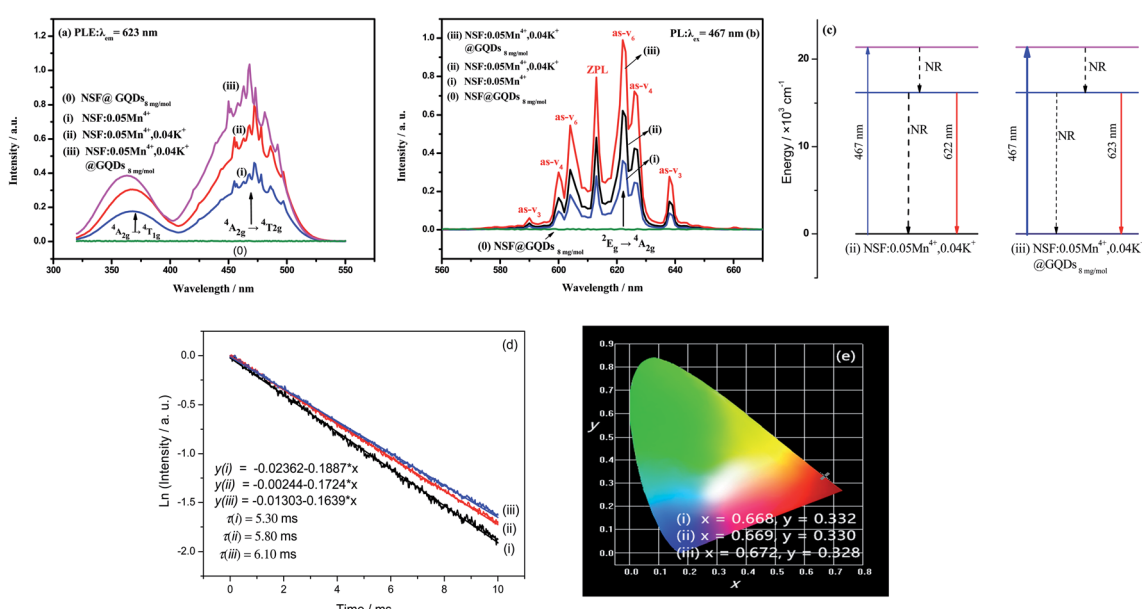

Fig. 3 Luminescent properties of four samples, (0) NSF@GQDs$_{8 mg mol^{-1}}$, (i) NSF:0.05Mn^{4+}, (ii) NSF:0.05Mn^{4+},0.04K$^+$, and (iii) NSF:0.05Mn^{4+},0.04K$^+$@GQDs$_{8 mg mol^{-1}}$: (a) PLE spectra, (b) PL spectra, (c) diagram of energy level transition induced by GQDs, (d) decay curves, and (e) CIE chromaticity diagrams.

It can be seen from Fig. 2e that the two samples are composed of elements of Na, K, Mn, F, Si, C and O, where C and O come from the GQDs and adsorbed CO_2 and H_2O, respectively. The high-resolution XPS of Mn 2p (Fig. 2f and g) show that two peaks of Mn 2p centered at about 647 and 658 eV, which can be attributed to Mn^{4+} from K_2MnF_6.[34,35]

The FTIR spectra of samples (ii) and (iii) and GQDs are illustrated in Fig. 2h. The spectrum of GQDs shows a characteristic peak at 1637 cm^{-1}, which is attributed to the C=C vibration.[36] Fig. 2h shows that samples (ii) and (iii) also have a peak at 1637 cm^{-1}, but the peak in the former is a weak, whereas that in the latter is slightly stronger. The former peak can be attributed to the C=O vibration peak of CO_2 (ref. 36) adsorbed by the sample in air, whereas that of the latter can be attributed to the overlapping peaks of the C=C vibration peak of GQDs[36] and the C=O vibration peak of CO_2. Thus, the EDS, XPS and FTIR results confirm that GQDs were coated on the surface of sample (iii).

3.2 Luminescent properties at room temperature

Fig. 3 shows the luminescent properties of the three samples, (i) NSF:$0.05Mn^{4+}$, (ii) NSF:$0.05Mn^{4+},0.04K^+$, and (iii) NSF:$0.05Mn^{4+},0.04K^+$@GQDs$_{8 \text{ mg mol}^{-1}}$. It can be seen in Fig. 3a and b that: (a) the PLE and PL spectra of sample (i) indicate that Mn^{4+} was successfully doped in the NSF, which is supported by results shown in Table 1 and Fig. 1. (b) The PLE and PL intensities of sample (ii) are 1.72 times that of sample (i), indicating

that the PLE and PL intensities were enhanced by the doping of K^+. Furthermore, the doping of K^+ is supported by results shown in Table 1, Fig. 1 and 2. (c) The PLE and PL intensities of sample (iii) are 1.50 times that of sample (ii), illustrating that the coating of GQDs further enhanced the PLE and PL intensities. The coating of GQDs is also supported by the results shown in Fig. 2.

It is well known that GQDs have large conjugated π bonds and can coordinate with Mn^{4+} and other transition metal ions. Thus, under the promotion of the coordination between GQDs and Mn^{4+}, the coating of GQDs not only enhances the absorption of blue light, but increases the radiative transition probability and decreases the non-radiative transition probability for the $^2E_g \rightarrow {}^4A_{2g}$ transition. The luminescent-enhanced mechanism induced by the coating of GQDs is illustrated in Fig. 3c, which is supported by the results shown in Fig. 3a and b.

All three samples have normal excitation bands and emission bands (Fig. 3a and b), where the main peak positions for the bands of the samples are basically the same. In the PLE spectra, two intense broad excitation bands are located at ~360 and ~467 nm, which are assigned to the spin-allowed $^4A_{2g} \rightarrow {}^4T_{1g}$ and $^4A_{2g} \rightarrow {}^4T_{2g}$ transitions of Mn^{4+},[22,23] respectively. Upon excitation by blue light with a wavelength of 467 nm, the emission spectra of the samples are composed of several sharp peaks, which are mainly distributed in the spectral region of 600–660 nm, with the strongest peak located at ~622 nm. The sharp emission peaks are attributed to the spin-forbidden ^2E_g
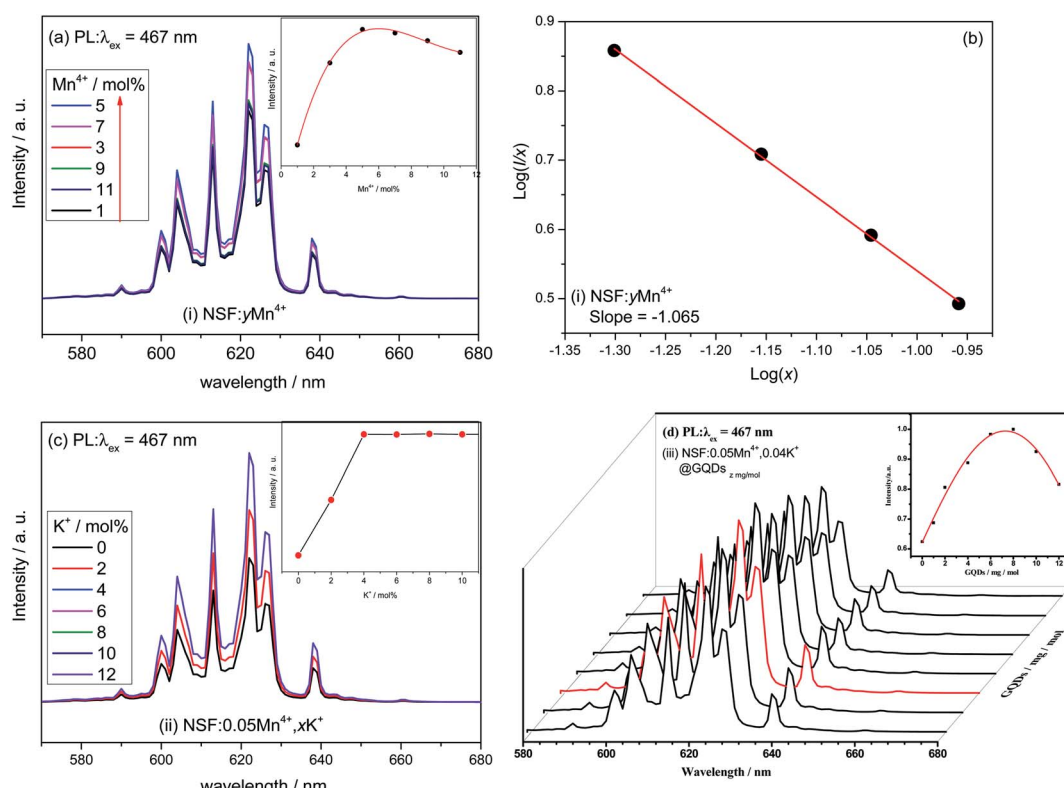

Fig. 4 Luminescent properties of NSF:yMn^{4+}, NSF:$0.05Mn^{4+},xK^+$ and NSF:$0.05Mn^{4+},0.04K^+$@GQDs$_{z \text{ mg mol}^{-1}}$: (a), (c) and (d) PL spectra and (b) related line type of multipolar interaction.

$\rightarrow$ $^4A_{2g}$ d–d transition of Mn^{4+},[37,38] which is activated by the $[MnF_6]^{2-}$ vibronic modes.[39] The details of the vibronic modes are as follows: 590 (as-v_3), 600 (as-v_4), 604 (as-v_6), 613 (ZPL), 622 (s-v_6), 626 (s-v_4) and 638 nm (s-v_3).

Fig. 3d shows the decay curves of the three samples. The curves can be fitted by a linear function with a constant term, and the lifetimes of samples (i)–(iii) are 5.30, 5.80 and 6.10 ms, respectively.

Theoretically, the luminescence lifetime is affected by the energy transfer process. In addition, it is well known that GQDs have large conjugated π bonds, and thus they can coordinate with Mn^{4+} by using the π bond as electron donor. Accordingly, the lifetime of sample (iii) increased under the promotion of the coordination between the GQDs and Mn^{4+}, where Mn^{4+} is the acceptor. Thus, the results in Fig. 3d indicate that energy transfer occurs from GQDs to Mn^{4+}.

The internal quantum yield (QY$_i$) of the sample was measured using an Edinburgh FL S980 fluorescence spectrophotometer with an integrating sphere. Eqn (3) was used to calculate the QY$_i$:[40]

$$QY_i = \frac{\int L_{emission}}{\int E_{blank} - \int E_{sample}} \quad (3)$$

where $L_{emission}$ is the emission spectrum of the sample, E_{sample} is the spectrum of the light used to excite the sample, and E_{blank} is the spectrum of the light used for excitation with only the empty powder vessel (without the sample) in the sphere. The QY$_i$ of samples (i)–(iii) was calculated to be 69.65, 88.95 and 99.03%, respectively, where the QY$_i$ of sample (iii) is higher than that of K$_2$SiF$_6$:Mn^{4+} (92%).[26] In general,[41] the QY$_i$ of K$_2$TiF$_6$:Mn^{4+} or Na$_2$TiF$_6$:Mn^{4+} is larger than that of K$_2$SiF$_6$:Mn^{4+} or Na$_2$SiF$_6$:-Mn^{4+}, where that of the former can be close to 100%. The results show that the coating of GQDs can increase the QY$_i$ of the Na$_2$SiF$_6$:Mn^{4+} samples, making their values similar to that of the K$_2$TiF$_6$:Mn^{4+} samples.[26,41]

By using the emission spectrum data of samples (i)–(iii) (Fig. 3b), the chromaticity coordinates of the samples were calculated using the "CIE1931 Chromaticity Coordinate Calculation" software, and the results (Fig. 3e) are as follows: (a) $x = 0.668$, $y = 0.332$ for sample (i), (b) $x = 0.669$, $y = 0.330$ for sample (ii), and (c) $x = 0.672$, $y = 0.328$ for sample (iii). It can be seen from Fig. 3e that the three points of the samples are almost overlapping, indicating that their color difference is very small.

Moreover, the color purities of the three samples were calculated using eqn (4):[42,43]
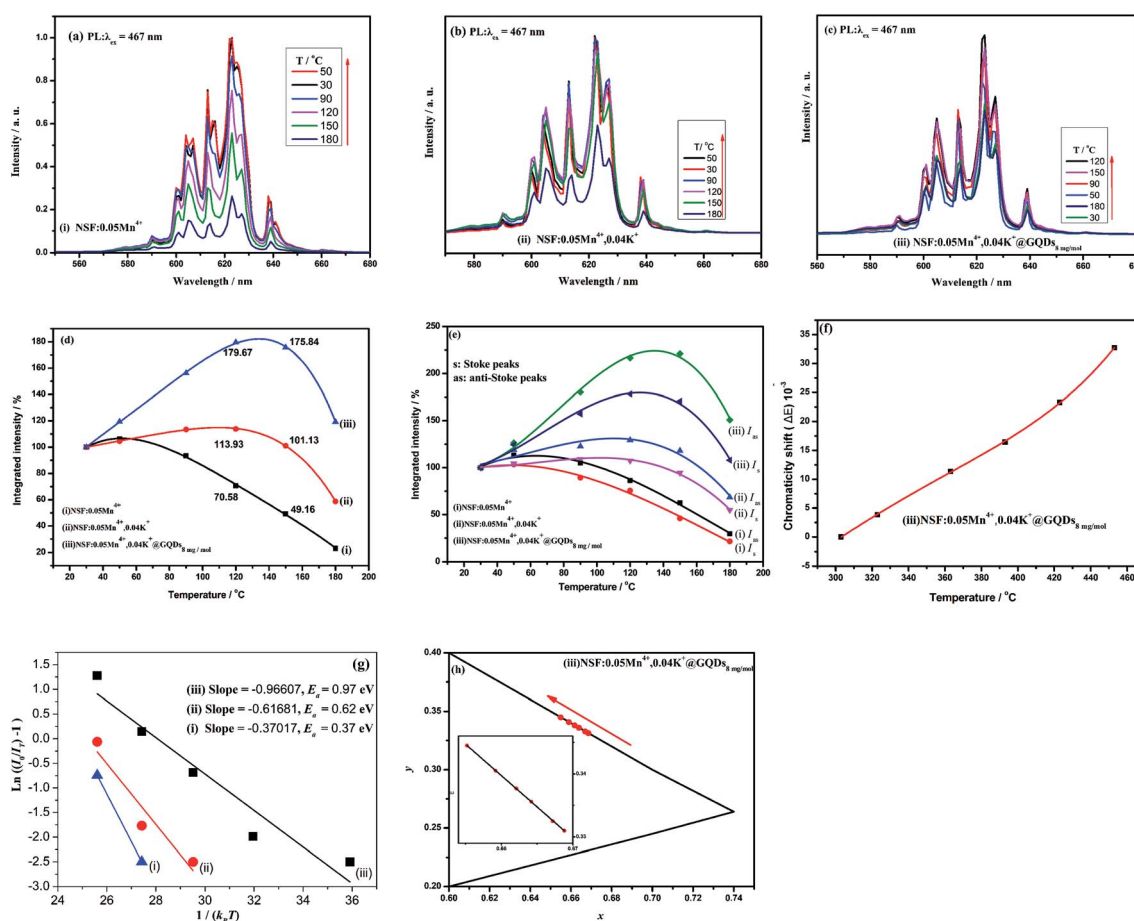
Fig. 5 PL performances of the three samples at different temperatures, (i) NSF:0.05Mn^{4+}, (ii) NSF:0.05Mn^{4+},0.04K$^+$, (iii) NSF:0.05Mn^{4+},0.04K$^+$@GQDs$_{8\text{ mg mol}^{-1}}$: (a), (b), and (c) PL spectra. (d) Integrated intensity curve. (e) Integrated intensity curves of Stoke and anti-Stoke peaks. (f) Chromaticity shift of sample (iii). (g) E_a curves. (h) CIE color coordinates of sample (iii).

$$CP = \frac{\sqrt{(x - x_i)^2 + (y - y_i)^2}}{\sqrt{(x_d - x_i)^2 + (y_d - y_i)^2}} \times 100\% \tag{4}$$

where (x, y) are the color coordinates of the sample, that is: (a) $x = 0.668$, $y = 0.332$ for sample (i), (b) $x = 0.669$, $y = 0.330$ for sample (ii), and (c) $x = 0.672$, $y = 0.328$ for sample (iii). (x_i, y_i) are the CIE of an equal-energy illuminant with a value of (0.33, 0.33), and (x_d, y_d) are the chromaticity coordinates corresponding to the dominant wavelength of the light source (the chromaticity coordinates of excitation were calculated to be $x_d = 0.1267$ and $y_d = 0.0534$ under excitation of 467 nm). The color purities of the three samples were determined to be: 98.43%, 98.78%, and 99.63% for samples (i)–(iii), respectively. These results indicate that the color purity of sample (ii) is slightly higher than that of sample (i), and that of sample (iii) is the closest to 100%.

3.3 Luminescent properties of NSF:yMn^{4+}, NSF:0.05Mn^{4+},xK$^+$, and NSF:0.05Mn^{4+},0.04K @GQDs$_{z\ mg\ mol^{-1}}$

The effect of the Mn/(Mn + Si) molar ratio (y = molar ratio of Mn/(Mn + Si)) on the luminescent properties is shown in Fig. 4a. Fig. 4a shows that the influence of the Mn/(Mn + Si) molar ratio on the PL intensity is parabola curve with a maximum. Firstly, the PL intensities of the samples increased with an increase in y, and achieved a max value at $y = 5\%$, and then declined when y is larger than 5% due to concentration quenching.

To further explore the concentration quenching mechanism of Mn^{4+} in sample (i), the critical distance (R_c) between the Mn^{4+} ions was calculated using eqn (5).[44]

$$R_c \approx 2\left[\frac{3V}{4\pi x_c N}\right]^{1/3} \tag{5}$$

where V is the unit cell volume of the sample, x_c is the critical concentration of Mn^{4+}, and N is the number of sites that activators can substitute per unit. When $R_c > 5$ Å, the non-radiative energy transfer is attributed to the multipolar interaction mechanism, whereas the energy transfer belongs to the exchange interaction mechanism when $R_c < 5$ Å. For sample (i) (NSF:0.05Mn^{4+}), $V = 342.75$ Å, $x_c = 5.0\%$, and $N = 3$, the calculated R_c is 16.34, indicating that the energy transfer between Mn^{4+} in sample (i) is not the exchange interaction mechanism, but the multipolar interaction mechanism.

The related type of multipolar interaction between Mn^{4+} in NSF:0.05Mn^{4+} can be estimated according to eqn (6).[45]

$$I/x = K[1 + \beta(x)^{\theta/3}]^{-1} \tag{6}$$

where K and β are constant parameters for the same excitation condition, I is the emission intensity of Mn^{4+}, and x is the concentration of Mn^{4+}, which is not less than x_c. The θ values of the exchange interaction, the dipole–dipole, dipole–quadrupole and quadrupole–quadrupole interaction are 3, 6, 8, and 10, respectively.[46]

Fig. 4b shows that the dependence of log(I/x) on log(x) for the NSF:xMn^{4+} samples can be fitted by a straight line, where the slope of the line is −1.065. The corresponding θ calculated with

the slope is 3.20, which is close to 3. The result indicates that the concentration quenching of Mn^{4+} in the NSF:xMn^{4+} samples may be dominated by the exchange interaction.

Based on NSF:0.05Mn^{4+}, the effect of the K/(Mn + Si) molar ratio (x = molar ratio of K/(Mn + Si)) on the luminescent properties was explored, as shown in Fig. 4c. Fig. 4c shows that the influence of x on the PL intensity is a stepped curve. Firstly, the PL intensities of the samples linearly increased with an increase in x, achieving a value of $x = 4\%$, and then basically remained unchanged.

Based on NSF:0.05Mn^{4+},0.04K$^+$, the enhancement effect induced by different concentrations of GQDs (z) was explored, as shown in Fig. 4d. Fig. 4d shows that the effect of concentration of GQDs on the PL intensities is a parabola with a maximum value. Firstly, the PL intensities of the samples were enhanced with an increase in the concentration of GQDs, reaching the maximum value at $z = 8$ mg mol^{-1}, and then decreased when z is larger than 8 mg mol^{-1} due to concentration quenching. As shown in Fig. 4d, the shapes of the PL spectra are not obviously affected by the concentration of GQDs.

3.4 Thermal stability analyses

The luminescent thermal stability of phosphors used in WLEDs is an important parameter for phosphors because the processing and operating temperature of the LED chip is often as high as 150 °C.[11,47] Thus, the luminescent thermal performances of the three samples (i)–(iii) ((i) NSF:0.05Mn^{4+}, (ii) NSF:0.05Mn^{4+},0.04K$^+$, and (iii) NSF:0.05Mn^{4+},0.04K$^+$@GQDs$_{8\ mg\ mol^{-1}}$) at different temperatures are shown in Fig. 5. Fig. 5a–c show that temperature strongly affects the integrated PL intensities of the three samples, where their PL peaks are broadened with an increase in temperature, but the wavelengths of their emission peaks do not shift with an increase in temperature. The curves of the integrated PL intensities (580−680 nm) of the three samples at different temperatures are shown in Fig. 5d. Fig. 5d illustrates that the curves of the three samples are all parabola curves with maximum values, showing that there are different degrees of thermal quenching effects[49–52] for the samples. The details of the three curves are as follows: firstly, the integrated PL intensities of the three samples are enhanced with an increase in temperature, reaching their maximum values, and then decreased when the temperature was higher than the maximum temperatures. The maximum temperatures of samples (i)–(iii) are 90.0 °C, 120.0 °C and 137.5 °C, respectively. Fig. 5d also indicates that after five cycles of testing (30–180 °C), the three curves remained basically unchanged. The results suggest that the luminescent thermal stability and chemical thermal stability of the three samples are high. There are also obvious differences between these three curves. (a) For sample (i), the integrated PL intensities at 120 °C, 150 °C and 180 °C are 75.2%, 49.2%, and 23.1% of the initial value at 25 °C, respectively. (b) For sample (ii), the integrated PL intensities at 120 °C, 150 °C and 180 °C are 113.9%, 101.1% and 58.7% of the initial value at 25 °C, respectively. (c) For sample (iii), the integrated PL intensities of 120 °C, 150 °C and 180 °C are 179.7%, 175.8% and 119.3% of the initial value at 25 °C, respectively. It can

be seen that after the coating of GQDs, the negative thermal quenching was obviously enhanced.

It has been reported that negative thermal quenching behavior occurred for several Mn^{4+}-doped phosphors (Table 2).[11,12,47,52,53] These phosphors include α-K_3AlF_6:Mn^{4+} prepared *via* a cation-exchange method,[11] K_2SiF_6:xMn^{4+} obtained by an HF-free hydrothermal method,[45] K_2SiF_6:Mn^{4+} synthesized *via* a two-step wet-chemical method at a low temperature of $-16\ °C$,[53] $CsMoO_2F_3$:Mn^{4+} synthesized *via* simple coprecipitation,[12] and K_2SiF_6:Mn^{4+}@GQDs obtained *via* cation exchange method and room temperature coating method in our previous work.[52]

In comparison, the negative thermal quenching of sample (iii) at 150 °C is the second largest one compared to that of the five above-mentioned samples. Therefore, when applied for WLEDs, sample (iii) will have enough red emission intensity at 150 °C. In addition, in most cases, the luminescence of Na_2SiF_6:Mn^{4+} synthesized *via* different methods does not have negative thermal quenching. However, the results herein and our previous work[31] show that K_2SiF_6:Mn^{4+} coated by GQDs is easy to obtain negative thermal quenching. Therefore, the method presented herein is an effective way to obtain Mn^{4+}-doped fluorides with high thermal stability.

To reveal the mechanism of negative thermal quenching, the change of the integrated intensities of the Stokes and anti-Stokes peaks of samples (i)–(iii) with an increase in temperature was studied in detail. The change in the integrated intensities of the Stokes and anti-Stokes peaks of samples (i)–(iii) at different temperatures is shown in Fig. 5e. Fig. 5e shows that with an increase in temperature, the curves of the integrated intensities of the anti-Stokes transitions (W_a) and Stokes transitions (W_s) are all parabolas with their maximums, but the W_a curve is higher than the W_s curve. The curves reach their tops when the temperature is 50 °C, 120 °C and 137 °C for samples (i)–(iii), respectively. These negative thermal quenching phenomena can be described using eqn (7) and (8):[41]

$$W_s(T) = D \cdot \frac{\exp\left(\frac{\hbar\omega}{kT}\right)}{\exp\left(\frac{\hbar\omega}{kT}\right) - 1} \quad (7)$$

$$W_a(T) = D \cdot \frac{1}{\exp\left(\frac{\hbar\omega}{kT}\right) - 1} \quad (8)$$

where $\hbar\omega$ is the energy of the coupled vibronic mode, D is the proportional coefficient, T is temperature and k is the Boltzmann constant. The equations indicate that W_a and W_s would be enhanced with an increase in temperature. Furthermore, the equations also show that W_a will rise more quickly than W_s with an increase in temperature increase. The integrated emission intensities of the samples (Fig. 5d) also reached the maximum at the same temperature, which are about 106%, 114% and 183% of the initial values at 25 °C of the three samples, respectively. Meanwhile, the integrated emission intensity of sample (iii) at 180 °C (119.3%) is still higher than the initial value at 25 °C.

Eqn (7) and (8) suggest that the major mechanism of the negative thermal quenching for the three samples can be attributed to the phonon-induced radiative transition probability increasing more rapidly than that of the non-radiative transition probability. Briefly, part of thermal energy is changed into light radiative energy by the phonons.

Furthermore, given that GQDs have a large conjugated π bond, they can coordinate with Mn^{4+} ions by using the π bond as an electron donor. Under the promotion of the coordination, the negative thermal quenching of sample (iii) is much larger than that of samples (i) and (ii).

To further understand the temperature effect on the luminescent properties, the chromaticity shift (ΔE) for the sample at different temperatures was calculated using the eqn (9) (ref. 53–55) as follows:

$$\Delta E = \sqrt{\left(u'_t - u'_0\right)^2 + \left(v'_t - v'_0\right)^2 + \left(w'_t - w'_0\right)^2} \quad (9)$$

where $u' = 4x/(3 - 2x + 12y)$, $v' = 9y/(3 - 2x + 12y)$ and $w' = 1 - u' - v$. u' and v' are the chromaticity coordinates in v' and u' uniform color space, x and y are the chromaticity coordinates in the CIE 1931 color space, and 0 and t are the chromaticity shift at 300 K and a given temperature.

Fig. 5f shows that the dependence of ΔE on temperature for sample (iii) (NSF:0.05Mn^{4+},0.04K^+@GQDs$_{8\ mg\ mol^{-1}}$) is a monotonically rising nonlinear curve, where ΔE increases with an increase in temperature. According to this curve, the value of ΔE at 175 °C is 30.78×10^{-3}. Thus, the ΔE of sample (iii) at 175 °C is smaller than that of CSASNE (44×10^{-3} at 175 °C),[47] indicating that it can meet the requirements of WLEDs.

The activation energy (E_a) of thermal quenching for the samples was also calculated using eqn (10). Eqn (11) can be transformed from eqn (10) (ref. 56 and 57) as follows:

$$I_T = \frac{I_0}{1 + A \exp\left(-\frac{E_a}{k_B T}\right)} \quad (10)$$

$$\ln\left(\frac{I_0}{I_T} - 1\right) = \ln A - \frac{E_a}{k_B T} \quad (11)$$

where I_0 is the initial emission intensity and I_T is the intensity at different temperatures. A is a constant, and k_B is the Boltzmann
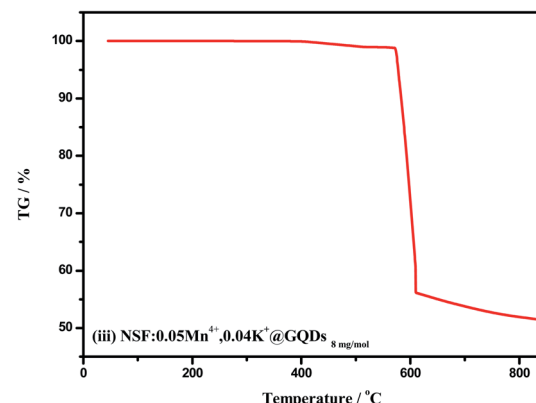

Fig. 6 TG of sample (iii) (NSF:0.05Mn^{4+},0.04K^+@GQDs$_{8\ mg\ mol^{-1}}$).
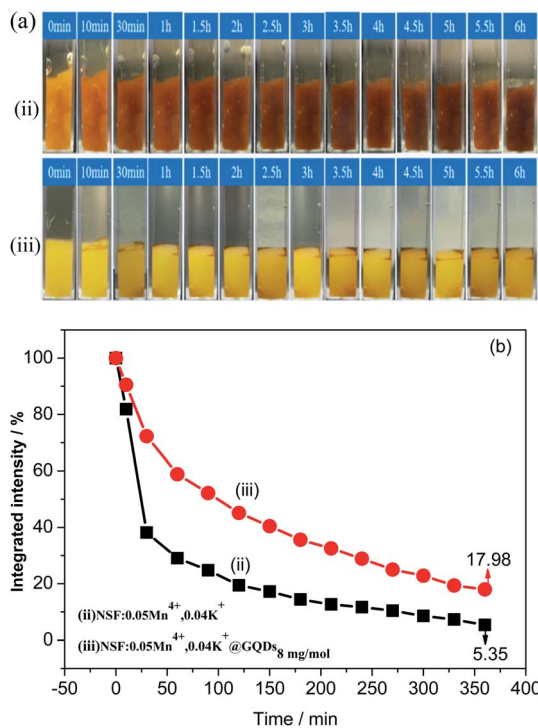
Fig. 7 Water resistance test of two samples: (ii) NSF:0.05Mn^{4+},0.04K^{+} and (iii) NSF:0.05Mn^{4+},0.04K^{+}@GQDs$_{8\text{ mg mol}^{-1}}$: (a) photographs under natural light and (b) PL integrated intensities with different soaking times in water.

constant (8.617×10^{-5} eV K^{-1}). E_a can be obtained from the slope of eqn (11), as shown in Fig. 5g. According to the slopes of the three lines in Fig. 5g, the E_a values for samples (i)–(iii) were determined to be 0.37, 0.62 and 0.97 eV, respectively, indicating that E_a effectively increased by coating of GQDs.

Fig. 5h shows the CIE color coordinates of sample (iii) at different temperatures. It can be seen from Fig. 5h that there is a slight shift in the color coordinates in the red region, which may be caused by the slight broadening of the sharp red emission peaks. However, this result shows that the color stability of sample (iii) is good.

The TG curve of sample (iii) is shown in Fig. 6. The TG curve below 1000 °C has one main step. The mass loss begins at about 80 °C and ends at about 800 °C. Before 300 °C, the mass loss is only 0.97%, which corresponds to the loss of adsorbed water. It can be seen from Fig. 6 that the sample decomposed rapidly at 560 °C, showing that the sample has high chemical thermal stability. Thus, it has sufficient chemical thermal stability at the working temperature of WLEDs (about 150 °C).

3.5 Water resistance

It is well known that the water resistance and thermal stability of samples are crucial properties.[13–15,55] The water resistance test of two samples: (ii) NSF:0.05Mn^{4+},0.04K^{+} and (iii) NSF:0.05Mn^{4+},0.04K^{+}@GQDs$_{8\text{ mg mol}^{-1}}$ are shown in Fig. 7. As can be seen in Fig. 7a, the color of the two samples gradually darkened with an increase in the soaking time. The color of sample (ii) was darker than that of sample (iii) after immersion in deionized water for 360 min. Fig. 7b shows that the PL integrated intensities of the two samples changed with different
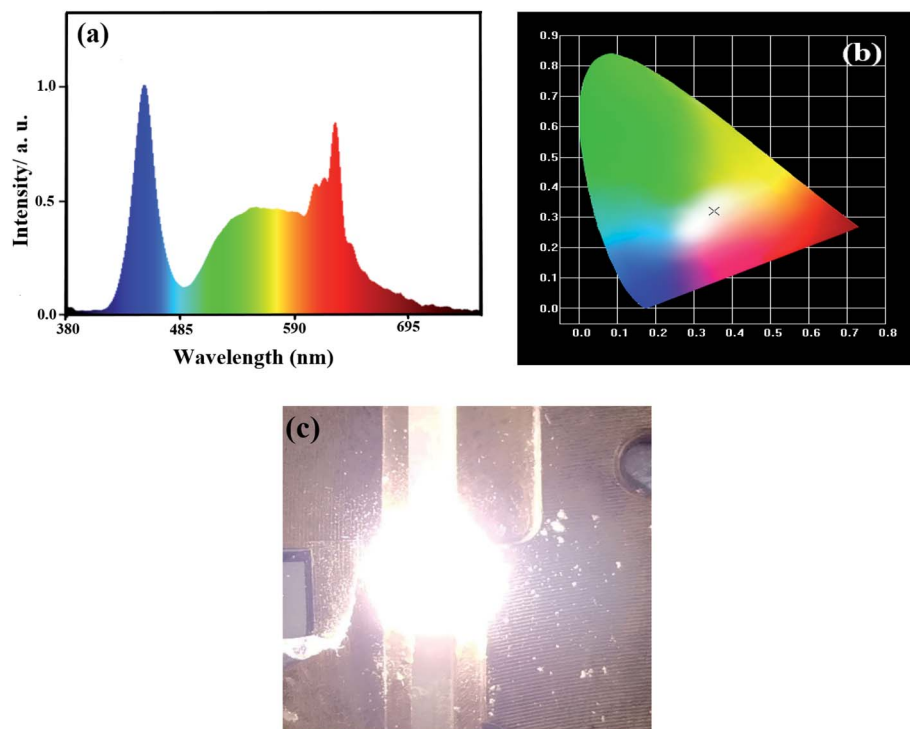

Fig. 8 Properties of prototype WLEDs fabricated using the mixed phosphors of NSF:0.05Mn^{4+},0.04K^{+}@GQDs$_{8\text{ mg mol}^{-1}}$ and YAG:Ce^{3+} based on an InGaN chip under a 20 mA drive current: (a) electroluminescence spectrum, (b) CIE chromaticity diagram and (c) luminescent photo.

Paper

soaking times in water. It can be seen from Fig. 7b that: (a) curve (iii) is higher than that of (ii), which indicates that the water resistance of the coated sample (sample (iii)) increased, but the increase was not significant. (b) The integrated PL intensities of the two samples rapidly decreased after immersion in water, and after immersion for 360 min, the intensities of samples (ii) and (iii) were only 5.35% and 17.98% of their original intensities, respectively.

The results herein show that the coating of GQDs can greatly improve the thermal stability of the samples, but has no significant effect on the water resistance. Therefore, how to improve the luminescent intensity, luminescent thermal stability and water resistance simultaneously needs to be further studied.

3.6 Performances of W-LEDs

Fig. 8 shows the performances of the prototype WLEDs assembled using the mixed phosphors of sample (iii) (NSF:$0.05Mn^{4+}$,$0.04K^+$@GQDs$_{8\ mg\ mol^{-1}}$) and YAG:Ce based on an InGaN chip under a 20 mA drive current. Fig. 7a shows the electroluminescent spectrum of the WLEDs. By using the spectrum data from Fig. 7a, the chromaticity coordinates of the WLEDs were calculated to be $x = 0.3536$ and $y = 0.3202$ (Fig. 7b), indicating that the WLEDs emit warm white light with luminescent efficiency = 101.9 lm W^{-1}, CCT = 4461 K and CRI = 90.6. Fig. 7c also shows that the WLEDs emit warm white light. Thus, sample (iii) can effectively improve the performances of WLEDs for indoor lighting.

4   Conclusions

In summary, a series of NSF:Mn^{4+},K$^+$@GQD phosphors was synthesized using the combination of a cation exchange method and simple hydrothermal coating method, and the optimal sample was NSF:$0.05Mn^{4+}$,$0.04K^+$@GQDs$_{8\ mg\ mol^{-1}}$. Double enhancement effects on luminescent intensity and thermal stability triggered by the coating of GQDs were observed for the optimal sample as follows: (a) its PL intensity is 1.72 times that of the uncoated control sample and (b) its luminescent thermal stability was greatly enhanced, with integrated PL intensities at 120 °C, 150 °C and 180 °C of 179.7%, 175.8%, 119.3% of the initial value at 25 °C, respectively. The mechanism for the negative-thermal quenching may be attributed to part of the thermal energy being changed into light radiative energy by phonons. The thermal stability analysis results also showed that the optimal sample exhibited color stability at the working temperature of WLEDs, suggesting that the sample can be applied for high-power WLEDs. Warm white light with luminescent efficiency = 101.9 lm W^{-1}, CCT = 4461 K and R_a = 90.6 was obtained from the prototype WLEDs using the mixed phosphors of the optimal sample and YAG:Ce based on an InGaN chip under a 20 mA drive current. Thus, this sample can be applied for blue light-based high-power warm WLEDs.

Conflicts of interest

There are no conflicts to declare.

Acknowledgements

References

1 G. Zhang, W. B. Chen, Y. A. Wang, X. Chen, Y. Y. Li, L. Zhao and Y. Q. Yang, Synthesis and luminescence properties of a novel deep red phosphor Li$_2$ZnTi$_3$O$_8$:Mn^{4+} for plant-cultivation, *Spectrochim. Acta, Part A*, 2020, **240**, 118567.

2 Y. X. Zou, L. X. Yu, Z. Y. Gao, J. L. Zhong, Q. H. Guo and Z. J. Liu, Synthesis, crystal structure, and photoluminescence of Eu^{2+}, Ce^{3+}, Mn^{2+} doped oxynitride phosphors, *Opt. Mater.*, 2019, **92**, 411–417.

3 Y. W. Zhu, L. Y. Cao, G. M. Brik, X. J. Zhang, L. Huang, T. T. Xuan and J. Wang, Facile synthesis, morphology and photoluminescence of a novel red fluoride nanophosphor K$_2$NaAlF$_6$:Mn^{4+}, *J. Mater. Chem. C*, 2017, **5**, 6420–6426.

4 Y. Arai and S. Adachi, Optical properties of Mn^{4+}-activated Na$_2$SnF$_6$ and Cs$_2$SnF$_6$ red phosphors, *J. Lumin.*, 2011, **131**, 0022–2313.

5 F. Hong, H. P. Xu, G. Pang, G. X. Liu, X. T. Dong and W. S. Yu, Optical characteristics, morphology evolution and thermal stability of novel red-emitting Mn^{4+}-activated K$_2$LiAl$_{1-y}$Ga$_y$F$_6$ solid solution phosphors for high-performance warm WLED, *J. Alloys Compd.*, 2020, **824**, 153818.

6 R. Hoshino and S. Adachi, Optical spectroscopy of ZnSiF$_6$·6H$_2$O:Mn^{4+} red phosphor, *J. Appl. Phys.*, 2013, **114**, 213502.

7 R. Hoshino and S. Adachi, Light-induced degradation in red-emitting ZnSiF$_6$·6H$_2$O:Mn^{4+} hydrate phosphor, *ECS J. Solid State Sci. Technol.*, 2014, **3**, R144–R149.

8 D. X. Shi, Z. B. Liang, X. Zhang, Q. Zhou, Z. L. Wang, M. M. Wu and Y. Q. Ye, Synthesis, structure and photoluminescence properties of a novel Rb$_2$NaAlF$_6$:Mn^{4+} red phosphor for solid-state lighting, *J. Lumin.*, 2020, **226**, 117491.

9 Y. K. Xu and S. Adachi, Properties of Na$_2$SiF$_6$:Mn^{4+} and Na$_2$GeF$_6$:Mn^{4+} red phosphors synthesized by wet chemical etching, *J. Appl. Phys.*, 2009, **105**, 013525.

10 Y. W. Zhu, Y. Liu, L. Huang, T. T. Xuan and J. Wang, Optimized photoluminescence of red phosphor K$_2$LiAlF$_6$:Mn^{4+} synthesized by a cation-exchange method, *Sci. China: Technol. Sci.*, 2017, **60**, 1458–1464.

11 E. H. Song, J. Q. Wang, J. H. Shi, T. T. Deng, S. Ye, M. Y. Peng, J. Wang, L. Wondraczek and Q. Y. Zhang, Highly efficient and thermally stable K$_3$AlF$_6$:Mn^{4+} as a red phosphor for

ultra-high- performance warm white light-emitting diodes, *ACS Appl. Mater. Interfaces*, 2017, **9**, 8805–8812.

12 O. M. ten Kate, Y. J. Zhao, K. M. B. Jansen, J. R. van Ommen and H. T. Hintzen, Effects of surface modification on optical properties and thermal stability of $K_2SiF_6:Mn^{4+}$ red phosphors by deposition of an ultrathin Al_2O_3 layer using gas-phase deposition in a fluidized bed reactor, *ECS J. Solid State Sci. Technol.*, 2019, **8**, R88–R96.

13 L. Huang, Y. Liu, J. B. Yu, Y. W. Zhu, F. J. Pan, T. T. Xuan, M. G. Brik, C. X. Wang and J. Wang, Highly stable $K_2SiF_6:Mn^{4+}@K_2SiF_6$ composite phosphor with narrow red emission for white LEDs, *ACS Appl. Mater. Interfaces*, 2018, **10**, 18082–18092.

14 C. Y. Jiang, L. H. Li, M. G. Brik, L. T. Lin and M. Y. Peng, Epitaxial growth *via* anti-solvent-induced deposition towards a highly efficient and stable Mn^{4+} doped fluoride red phosphor for application in warm WLEDs, *J. Mater. Chem. C*, 2019, **7**, 6077–6084.

15 D. C. Huang, H. M. Zhu, Z. H. Deng, Q. L. Zou, H. Y. Lu, X. D. Yi, W. Guo, C. Z. Lu and X. Y. Chen, Moisture-resistant Mn^{4+}-doped core-shell-structured fluoride red phosphor exhibiting high luminous efficacy for warm white light-emitting diodes, *Angew. Chem., Int. Ed.*, 2019, **58**, 3843–3847.

16 T. C. Lang, T. Han, S. Q. Fang, J. Y. Wang, S. X. Cao, L. L. Peng, B. T. Liu, V. I. Korepanov and A. N. Yakovlev, Improved phase stability of the metastable $K_2GeF_6:Mn^{4+}$ phosphors with high thermal stability and water-proof property by cation substitution, *Chem. Eng. J.*, 2020, **380**, 122429.

17 Z. L. Wang, Z. Y. Yang, H. Y. Tan, M. G. Brik, Q. Zhou, G. Chen and H. B. Liang, Red-emitting phosphor $Rb_2TiF_6:Mn^{4+}$ with high thermal-quenching resistance for wide color-gamut white light-emitting diodes, *Opt. Mater.*, 2017, **72**, 78–85.

18 S. G. He, F. F. Xu, T. T. Han, Z. Q. Lu, W. Wang, J. Q. Peng, F. Du, F. L. Yang and X. Y. Ye, A Mn^{4+}-doped oxyfluoride phosphor with remarkable negative thermal quenching and high color stability for warm WLEDs, *Chem. Eng. J.*, 2020, **392**, 123657.

19 T. Hu, H. Lin, F. Lin, Y. Gao, Y. Cheng, J. Xu and Y. Wang, Narrow-band red-emitting $KZnF_3:Mn^{4+}$ fluoroperovskites: insights into electronic/vibronic transition and thermal quenching behavior, *J. Mater. Chem. C*, 2018, **6**, 10845–10854.

20 C. Y. Jiang, M. G. Brik, L. H. Li, J. Peng, J. N. Wu, M. S. Molokeev, K. L. Wong and M. Peng, The electronic and optical properties of a narrow-band red-emitting nanophosphor $K_2NaGaF_6:Mn^{4+}$ for warm white light-emitting diodes, *J. Mater. Chem. C*, 2018, **6**, 3016–3025.

21 H. Cheng, F. Hong, G. Liu, D. Li, Q. Ma, X. Dong and W. Yu, Design, preparation, and optical characteristics of novel red phosphors $A_2NaInF_6:Mn^{4+}$ (A = K and NH_4) for improving the performance of WLED, *J. Lumin.*, 2019, **210**, 146–154.

22 H. Lin, T. Hu, Q. Huang, Y. Cheng, B. Wang, J. Xu, J. Wang and Y. S. Wang, Non-rareearth $K_2XF_7:Mn^{4+}$ (X = Ta, Nb): a highly-efficient narrow-band red phosphor enabling the

application in wide-color-gamut LCD, *Laser Photonics Rev.*, 2017, **11**, 1700148.

23 Q. Zhou, H. Tan, Y. Zhou, Q. Zhang, Z. Wang, J. Yan and M. Wu, Optical performance of Mn^{4+} in a new hexa-coordinated fluorozirconate complex of Cs_2ZrF_6, *J. Mater. Chem. C*, 2016, **4**, 7443–7448.

24 Y. M. Liu, T. M. Wang, Z. R. Tan, J. M. Meng, W. J. Huang, Y. H. Huang, S. Liao and H. X. Zhang, Novel emission bands of $Na_2TiF_6:Mn^{4+}$ phosphors induced by the cation exchange method, *Ceram. Int.*, 2019, **45**, 6243–6249.

25 S. Q. Meng, Y. Y. Zhou, W. Wan, S. Ye and Q. Y. Zhang, Facile *in situ* synthesis of zeolite-encapsulating $Cs_2SiF_6:Mn^{4+}$ for application in WLEDs, *J. Mater. Chem. C*, 2019, **7**, 1345–1352.

26 Z. Y. Hou, X. Y. Tang, X. F. Luo, T. L. Zhou, L. Zhang and R. J. Xie, A green synthetic route to the highly efficient $K_2SiF_6:Mn^{4+}$ narrow-band red phosphor for warm white light-emitting diodes, *J. Mater. Chem. C*, 2018, **6**, 2741–2746.

27 D. C. Huang, H. M. Zhu, Z. H. Deng, Q. L. Zou, H. Y. Lu, X. D. Yi, W. Guo, C. H. Lu and X. Y. Chen, Moisture-resistant Mn^{4+}-doped core-shell-structured fluoride red phosphor exhibiting high luminous efficacy for warm white LEDs-emitting diodes, *Angew. Chem., Int. Ed.*, 2019, **59**, 3843–3847.

28 A. K. Srivastava, V. Gupta, C. S. Dermally and A. Singh, Flexural strength enhancement in carbon-fiber epoxy composites through graphenenano-platelets coating on fibers, *Composites Part B*, 2019, **179**, 107539.

29 W. J. Zhang, X. F. Zou and J. F. Zhao, Preparation and performance of a novel graphene oxide sheets modified rare-earth luminescence material, *J. Mater. Chem. C*, 2015, **3**, 1294–1300.

30 G. Anoop, J. R. Rani, J. Lim, M. S. Jang, D. W. Suh, S. Kang, S. C. Jun and J. S. Yoo, Reduced graphene oxide enwrapped phosphors for long-term thermally stable phosphor converted white light emitting diodes, *Sci. Rep.*, 2016, **6**, 33993.

31 Y. L. Li, X. Zhong, Y. Yu, Y. M. Liu, S. Liao, Y. H. Huang and H. X. Zhang, H_2O_2-Free preparation of K2SiF6:Mn4+ and remarkable high luminescent thermal stability induced by coating with graphene quantum dots, *Mater. Chem. Phys.*, 2021, **260**, 124149.

32 Y. M. Liu, T. M. Wang, Z. P. Chen, K. Y. Chen, M. M. Guan, Y. H. Huang, S. Liao and H. X. Zhang, NaF induced enhancement of luminous efficiency in narrow-band redemitting $K_2TiF_6:Mn^{4+}@NaF$ phosphors, *J. Mater. Sci.: Mater. Electron.*, 2018, **29**, 12536–12542.

33 Y. Gao, Q. W. Long, R. Nong, T. M. Wang, H. X. Zhang, Y. H. Huang and S. Liao, Strain-induced enhancement of Eu^{3+} emission in red phosphor $NaMgPO_4:Eu^{3+}$, Al^{3+}, *J. Electron. Mater.*, 2017, **46**, 911–916.

34 B. V. Crist, *Handbooks of Monochromatic XPS Spectra Volume 1 - The Elements and Native Oxides [M]*, Mountain View, California, USA, 1999.

35 J. F. Moulder, J. Chastain and R. C. King Jr, Handbook of X-ray photoelectron spectroscopy: A reference book of standard spectra for identification and interpretation of XPS data, *Chem. Phys. Lett.*, 1979, **220**, 7–10.

36 Y. C. Zhao, L. J. Huang, Y. X. Wang, J. G. Tang, Y. Wang, J. X. Liu, L. A. Belfiore and M. J. Kipper, Synthesis of graphene oxide/rare-earth complex hybrid luminescent materials via π-π stacking and their pH-dependent luminescence, *J. Alloys Compd.*, 2016, **687**, 95–103.

37 M. G. Brik, S. J. Camardello and A. M. Srivastava, Influence of covalency on the Mn^{4+} $^2E_g \rightarrow {}^4A_{2g}$ emission energy in crystals, *ECS J. Solid State Sci. Technol.*, 2014, **4**, R39–R43.

38 Y. M. Liu, Y. L. Li, W. J. Huang, J. M. Meng, W. F. Liang, S. Sen, Y. H. Huang and H. X. Zhang, Enhancement of zero phonon line for Na_2TiF_6:Mn^{4+}, Li^+ phosphors induced by Li^+, *J. Mater. Sci.: Mater. Electron.*, 2019, **30**, 14646–14656.

39 L. P. Dong, L. Zhang, Y. C. Jia, B. Q. Shao, W. Lu, S. Zhao and H. P. You, Site occupation and luminescence of novel orange-red $Ca_3M_2Ge_3O_{12}$: Mn^{2+}, Mn^{4+} (M = Al, Ga) phosphors, *ACS Sustainable Chem. Eng.*, 2020, **8**, 3357–3366.

40 J. C. de Mello, H. F. Wittmann and R. H. Friend, An improved experimental determination of external photoluminescence quantum efficiency, *Adv. Mater.*, 1997, **9**, 230–232.

41 H. M. Zhu, C. C. Lin, W. Q. Luo, S. T. Shu, Z. G. Liu, Y. S. Liu, J. T. Kong, E. Ma, Y. G. Cao and R. S. Liu, Highly efficient non-rare-earth red emitting phosphor for warm white light-emitting diodes, *Nat. Commun.*, 2014, **5**, 4312.

42 Y. W. Zhu, L. Huang, R. Zou, J. H. Zhang, J. B. Yu, M. M. Wu, J. Wang and Q. Su, Hydrothermal synthesis, morphology and photoluminescent properties of an Mn^{4+}-doped novel red fluoride phosphor elpasolite K_2LiAlF_6, *J. Mater. Chem. C*, 2016, **4**, 5690–5695.

43 Y. W. Zhu, J. B. Yu, Y. Liu, M. G. Brik, L. Huang, T. T. Xuan and J. Wang, Photoluminescence properties of a novel red fluoride K_2LiGaF_6:Mn^{4+} nanophosphor, *RSC Adv.*, 2017, **7**, 30588–30593.

44 M. M. Zhu, Y. X. Pan, L. Q. Xi, H. Z. Lian and J. Lin, Design, preparation, and optimized luminescence of a dodec-fluoride phosphor $Li_3Na_3Al_2F_{12}$:Mn^{4+} for warm WLED applications, *J. Mater. Chem. C*, 2017, **5**, 10241–10250.

45 M. G. Brik, S. J. Camardello, A. M. Srivastava, N. M. Avram and A. Suchocki, Spin-forbidden transitions in the spectra of transition metal ions and nephelauxetic effect, *ECS J. Solid State Sci. Technol.*, 2016, **5**, R3067–R3077.

46 Y. Tian, B. J. Chen, R. N. Hua, H. Y. Zhong, L. H. Cheng, J. S. Sun, W. L. Lu and J. Wan, Synthesis and characterization of novel red emitting nanocrystal Gd_6WO_{12}:Eu^{3+} phosphors, *Phys. B*, 2009, **404**, 3598–3601.

47 L. Huang, Y. W. Zhu, X. J. Zhang, R. Zou, F. J. Pan, J. Wang and M. M. Wu, HF-free hydrothermal route for synthesis of highly efficient narrow-band red emitting phosphor $K_2Si_{1-x}F_6$: xMn^{4+} for warm white light-emitting diodes, *Chem. Mater.*, 2016, **28**, 1495–1502.

48 D. P. Cui, Z. Song, Z. G. Xia, Q. L. Liu, Y. M. Liu, Y. L. Li, Y. T. Feng and J. M. Meng, Synthesis, structure and luminescence of $SrLiAl_3N_4$:Ce^{3+} phosphor, *J. Lumin.*, 2018, **199**, 271–277.

49 B. Peng, K. X. Song, H. W. Wang, S. S. Zhang, W. T. Su and Z. Q. Cheng, Investigation on Ce^{3+} luminescence from different crystallographic sites, self energy transfer and abnormal thermal stability of nitrided $Ba_9Y_2Si_6O_{24}$:Ce^{3+} phosphor for W-LEDs, *Ceram. Int.*, 2018, **44**, 6584–6589.

50 Z. B. Tang, G. Y. Zhang and Y. H. Wang, Design and development of a bluish-green luminescent material ($K_2HfSi_3O_9$:Eu^{2+}) with robust thermal stability for white light-emitting diodes, *ACS Photonics*, 2018, **5**, 2330–4022.

51 J. Y. Zhong, W. R. Zhao, F. Du, J. Wen, W. D. Zhuang, R. H. Liu, C. K. Duan, L. G. Wang and K. Lin, Identifying the emission centers and probing the mechanism for highly efficient and thermally stable luminescence in the $La_3Si_6N_{11}$:Ce^{3+} phosphor, *J. Phys. Chem. C*, 2018, **122**, 1932–7447.

52 Y. M. Liu, Y. L. Li, Y. T. Feng, J. M. Meng, S. Liao, Y. H. Huang and H. X. Zhang, Effects of graphene quantum dots coating on the luminescence properties of K_2SiF_6:Mn^{4+} red emitting phosphors, *J. Mater. Sci.: Mater. Electron.*, 2020, **31**, 444–456.

53 F. Tang, Z. C. Su, H. G. Ye, W. P. Gao, X. Q. Pan and S. J. Xu, Large negative- thermal- quenching effect in phonon-induced light emissions in Mn^{4+}-activated fluoride phosphor for warm-white light-emitting diodes, *ACS Omega*, 2018, **3**, 13704–13710.

54 X. L. Zhang, L. Huang, F. J. Pan, M. M. Wu, J. Wang, Y. Chen and Q. Su, Highly thermally stable single-component white-emitting silicate glass for organic-resin-free white-light-emitting diodes, *ACS Appl. Mater. Interfaces*, 2014, **6**, 2709–2717.

55 X. J. Zhang, J. B. Yu, J. Wang, C. B. Zhu, J. H. Zhang, R. Zou, B. F. Lei, Y. L. Liu and M. M. Wu, Facile preparation and ultrastable performance of single-component white-light-emitting phosphor-in-glass used for high-power warm white LEDs, *ACS Appl. Mater. Interfaces*, 2015, **7**, 28122–28127.

56 H. Chen, H. Lin, Q. M. Huang, F. Huang, J. Xu, B. Wang, Z. B. Lin, J. C. Zhou and Y. S. Wang, A novel double-perovskite Gd_2ZnTiO_6:Mn^{4+} red phosphor for UV-based W-LEDs: structure and luminescence properties, *J. Mater. Chem. C*, 2016, **4**, 2374–2381.

57 L. Y. Wang, E. H. Song, T. T. Deng, Y. Y. Zhou, Z. F. Liao, W. R. Zhao, B. Zhou and Q. Y. Zhang, Luminescence properties and warm white LED application of a ternary-alkaline fluoride red phosphor K_2NaAlF_6:Mn^{4+}, *Dalton Trans.*, 2017, **46**, 9925–9933.